

# Machine learning boosting the discovery of porous metamaterials with an abnormal thermal transport property

Cite as: Appl. Phys. Lett. **122**, 144102 (2023); doi: [10.1063/5.0137665](https://doi.org/10.1063/5.0137665)

Submitted: 5 December 2022 · Accepted: 19 March 2023 ·

Published Online: 7 April 2023



View Online



Export Citation



CrossMark

Yu Yang,  Yunshan Zhao,<sup>a)</sup>  and Lifa Zhang<sup>a)</sup> 

## AFFILIATIONS

Phonon Engineering Research Center of Jiangsu Province, Center for Quantum Transport and Thermal Energy Science, Institute of Physics Frontiers and Interdisciplinary Sciences, School of Physics and Technology, Nanjing Normal University, Nanjing 210023, China

**Note:** This paper is part of the APL Special Collection on Accelerate Materials Discovery and Phenomena.

<sup>a)</sup>Author to whom correspondence should be addressed: [phyzys@njnu.edu.cn](mailto:phyzys@njnu.edu.cn) and [phyzlf@njnu.edu.cn](mailto:phyzlf@njnu.edu.cn)

## ABSTRACT

Normally, the introduction of porous structures into materials can tune their thermal conductivity, showing great applications in thermal management and thermoelectric energy harvesting. However, the ability of disorder changing the thermal conductivity of porous materials has seldom been explored. In this work, we show that an introduction of disorder into the macroscopic porous materials with a certain porosity can lead to a desired effective thermal conductivity over a large range, where an abnormal enhancement of  $\sim 7.9\%$  and a normal reduction of  $\sim 44\%$  at room temperature are predicted by the machine-learning-optimized algorithm. All of these theoretical calculation results are further verified by our experiments performed in the current work by using the steady-state thermal flux method. Moreover, when these periodic units are artificially connected, a structural anisotropy up to 40 is achieved, which can be further used to adjust the direction of the thermal flux in a well-controlled way. Our work provides an efficient and convenient approach for designing high-performance porous materials with specific thermal conductivity and high structural anisotropy for various applications in thermal management.

Published under an exclusive license by AIP Publishing. <https://doi.org/10.1063/5.0137665>

The efficient management of heat is essential and challenging for many fast-developing industries unprecedentedly in recent years, such as thermal dissipation in the nano-level chip,<sup>1</sup> thermal management in the new energy vehicle,<sup>2</sup> the low-carbon-oriented thermal energy recovery management,<sup>3</sup> etc. A variety of strategies have been proposed recently to achieve high-performance thermal management in both macroscopic and microscopic thermal transport.<sup>4–6</sup> On the microscopic scale, the idea of “phonon engineering” has been employed to achieve various interesting thermal control phenomena, such as phonon coherence,<sup>7–9</sup> phonon localization,<sup>10</sup> phonon devices,<sup>11,12</sup> etc. Macroscopically, abundant thermal metamaterials, which are primary for designing the thermal conductivity of bulk materials, have been proposed and have great applications in various thermal functional devices.<sup>13–15</sup> Among the emerging various metamaterials, porous materials are normally explored as a simple one with rich physical properties. For a homogeneous and symmetric porous material, called phononic crystals (PCs),<sup>16</sup> the propagation of phonon wave in it will produce a phonon interference,<sup>17,18</sup> leading to a large reduction ( $\sim 10^2$  times reduction

compared to the bulk value) in its thermal conductivity,<sup>19–24</sup> and, thus, PCs have potential applications in thermoelectrics.<sup>25,26</sup>

An even disordered structure could be introduced into the porous materials, and it is expected that a further reduction in the thermal conductivity would be obtained in this way compared to that of the ordered structures.<sup>24,27–33</sup> However, Maire *et al.* demonstrated that the disorder in low dimensional silicon-on-insulator wafer could lead to an abnormal enhancement in thermal conductivity at 4 K, which is inconsistent with the previous results.<sup>34</sup> The origin is attributed to the fact that the greater the disorder is, the cutoff frequency of the coherent phonons is shifted to the low frequency regime, resulting in the existence of more high-frequency phonons and a further enhancement in thermal conductivity. All the subsequent calculations obtained contradictory results until Wei *et al.* used a genetic algorithm to seek out several configurations, where the introduction of the disorder structures could, indeed, enhance the thermal conductivity at 300 K.<sup>35</sup> However, the physical mechanism here is that rather than the assumptions of the wave like behavior of phonon, the abnormal

enhancement in the thermal conductivity is attributed to the particle behavior of phonons, which is closely related to the special pore arrangement. Although these interesting works show the potential application of disordered porous metamaterials, they focus on the low temperature and on the micro- or nano-scale, and for the macroscopic materials that are more applicable at room temperature or even higher temperature conditions, there is a lack of study yet.<sup>36–38</sup>

In this work, we demonstrate that in a macroscopic system, the thermal conductivity can be abnormally enhanced by introducing a suitable disorder. The configuration with abnormal enhancement ( $\sim 7.9\%$ ) and the normal reduction ( $\sim 44\%$ ) in the effective thermal conductivity (ETC) have been shown by using a multi-layer perceptron (MLP)<sup>39–49</sup> and the particle swarm optimization (PSO)

algorithm.<sup>50–53</sup> Unexpectedly, these two configurations are actually along the two directions of the same configuration with a structural anisotropy ratio around 2. An experimental measurement based on the steady thermal flux method is carried out to confirm the theoretical prediction. Moreover, by extending the configuration layer, a structure with an anisotropy ratio exceeding 40 is achieved, and the application of thermal control is further demonstrated in this study. Our work provides an effective way for the design of high-performance porous materials for thermal management applications.

A two-dimensional porous alumina sheet with a square side length of  $a = 4$  m is employed in our study, as shown in Fig. 1(a). Periodic pores with radius  $r = 0.3$  m are uniformly arranged along the  $x$  and  $y$  directions. The typical finite element method (FEM, Method

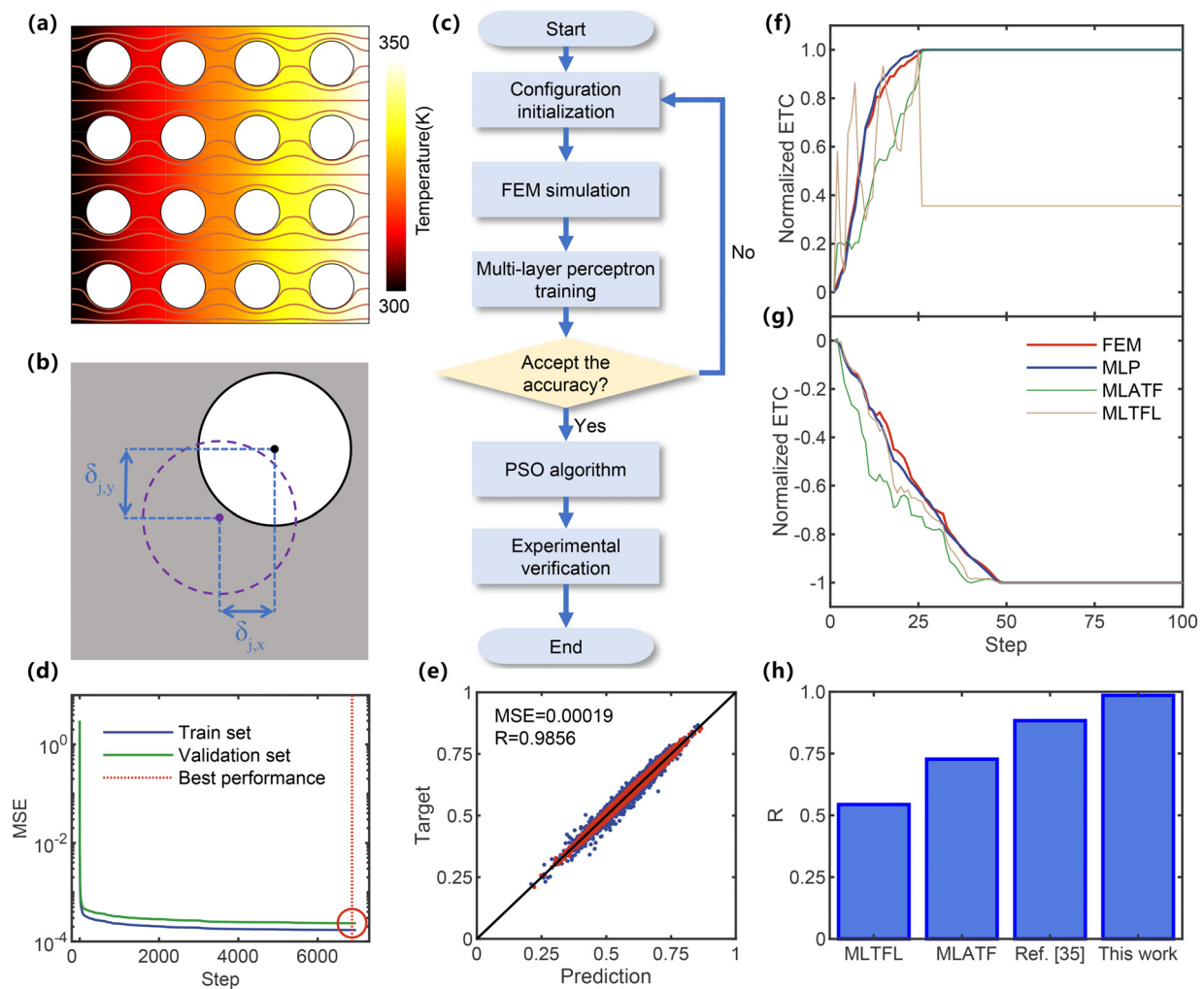


**FIG. 1.** Active learning, optimization, and performance comparison of MLP. (a) The temperature distribution and partial thermal flux line (brown curve) of the uniform arrangement configuration. (b) A schematic diagram of moving the pore to construct the disordered configuration. (c) A complete flow chart of the entire research. (d) The MSE of the training set and the validation set as two functions of the training step. The red circle marks the position of the optimal training performance. (e) The accurate ETC obtained by the FEM is a function of the predicted ETC by the MLP. The red scattered dots indicate the configuration with the lowest 90% absolute error, which implies that the remaining 10% configuration brings greater broadening. (f) and (g) The optimization process of the largest-ETC configuration and the smallest-ETC configuration by using the MLP and the PSO algorithm (blue curve). The red, green, and beige lines show the accurate value of the FEM, the predicted value of the MLATF method, and the predicted value of the MLTFL method for comparison, respectively. (h) The correlation coefficient histogram of the MLTFL method, MLATF method, artificial descriptor, and MLP.

S1) is employed to obtain the average thermal flux  $J$  of the entire porous material under the external thermal temperature difference  $\Delta T$ . The effective thermal conductivity  $\kappa_e$  can be calculated by Fourier's law, as follows:

$$\kappa_e = \frac{J}{\Delta T}. \quad (1)$$

Then, the position of each pore is randomly adjusted to construct a disordered configuration dataset for the subsequent study. As shown in Fig. 1(b), the displacement of the  $j$ -th pore in the  $x$  and  $y$  directions is denoted by  $\delta_{j,x}$  and  $\delta_{j,y}$ , respectively. We define the degree of disorder of the  $i$ -th configuration  $\delta_i$  as the maximum value of  $\delta_{j,x}$  and  $\delta_{j,y}$ . Initially, we investigate 2000 randomly generated configurations in different degrees of disorder, and their ETC is shown in Fig. S1. Different from that in the previous work, it is much convenient here to find the configurations with abnormal enhancement in ETC, especially for the high disorder case. The next question is why there is an abnormal enhancement in ETC at room temperature and at the macroscopic limit, and what is the limit for it. In order to better understand the calculation process, a complete flow chart is shown in Fig. 1(c).

Due to the fact that there are many parameters for each configuration, and that the complex coupling between these parameters together affects ETC, it is difficult to establish a direct function that accurately describes the configuration and its ETC. The multi-layer perceptron (MLP) is selected as the predictive model between the generation configuration and its ETC, considering its higher accuracy and greater universality than the previous artificial-guessed predictive models.<sup>39–42,44–46</sup> Here, the four-layer MLP is optimized by the back-propagation method, and its structure is shown in Fig. S2 (the detailed introduction in Method S2). To achieve the high accuracy, 55 000 random configurations and 7000 training steps are performed. The overall training process is shown in Figs. 1(d) and S3. We use the following mean square error (MSE) and correlation coefficient ( $R$ ) to evaluate the accuracy of MLP:

$$MSE = \frac{1}{n} \sum_{i=1}^n (y_i - \hat{y}_i)^2, \quad (2)$$

$$R = \frac{\sqrt{\sum_{i=1}^n (\hat{y}_i - \bar{y})^2}}{\sqrt{\sum_{i=1}^n (y_i - \bar{y})^2}}. \quad (3)$$

In Eqs. (2) and (3),  $y_i$  represents the accurate value by FEM,  $\hat{y}_i$  represents the predicted value by MLP, and  $\bar{y}$  represents the mean of  $y_i$ . The predicted ETC of the complete set based on the MLP is shown in Fig. 1(e), and the correlation coefficient  $R$  and the mean square error  $MSE$  of the MLP are 0.9856 and  $1.9 \times 10^{-4}$ , respectively. In particular, Figs. S4 and S5 show that the training set, the validation set, and the test set have a common high accuracy, implying that the issue of over-fitting does not exist in this highly accurate MLP.

The MLP well describes the relationship between configuration and its ETC, providing an opportunity to find the optimal disordered configuration. Since the candidate configurations are distributed in a continuous huge 32-dimensional space, which is quite intractable for the common optimization algorithm, the particle swarm optimization

(PSO) algorithm is employed in this work (Method S3). The 300 initial particles (configurations) are released in the high-dimensional parameter space, and then they keep moving toward the optimum state. Finally, around the 50th optimization step, the algorithm converges and shows a better disordered configuration, as shown in Figs. 1(f), 1(g), and S6. The schematic diagram of the configuration with the largest- and smallest-ETC obtained by the PSO is shown in the inset of Fig. 2. The largest-ETC is enhanced by 7.9% compared to that of the uniform arrangement, while the smallest-ETC is reduced by 44%. The relative change factor  $\mu$  is defined as follows:

$$\mu = \frac{\kappa_r - \kappa_u}{\kappa_u}. \quad (4)$$

Here,  $\kappa_r$  and  $\kappa_u$  represent the ETC of the random configuration and the uniform arrangement configuration, respectively. By comparing the optimal configurations, the largest- and smallest-ETC are actually along the two directions of the same configuration, with a structural anisotropy ratio of about 2. In this paper, the anisotropy ratio  $\gamma$  is defined as follows:

$$\gamma = \frac{\kappa_{e,y}}{\kappa_{e,x}}. \quad (5)$$

Here,  $\kappa_{e,x(or y)}$  represents the ETC along the  $x$  (or  $y$ ) direction. One conclusion in Fig. S7 is that as the disorder become greater, the accompanied anisotropy increases quickly, which possibly has a significant application in thermal management<sup>36–38</sup> and thermoelectric energy harvesting.<sup>54</sup> Compared with the previous work, the optimal

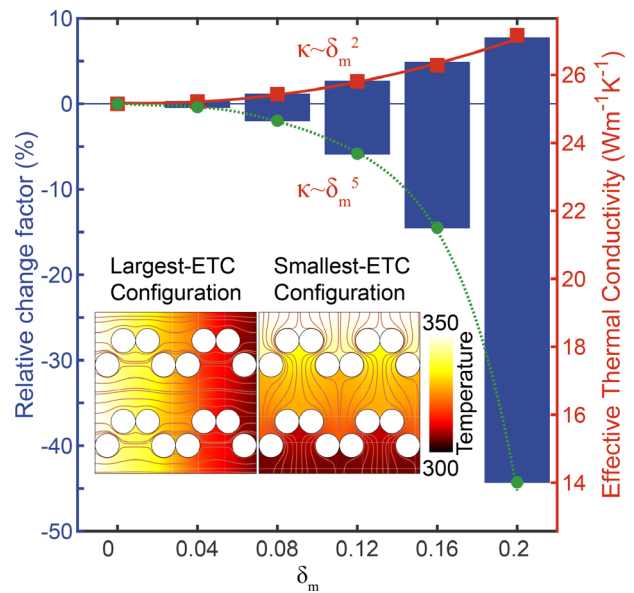


**FIG. 2.** The optimal disordered configuration in different degrees of disorder. The blue histogram shows the largest relative enhancement percentage and largest reduction percentage in different degrees of disorder. Red square and green circle scatters give the ETC of the largest- and smallest-ETC disordered configuration in different degrees of disorder. In the inset, we show the largest-ETC configuration and the smallest-ETC configuration in the disorder degree of 0.2, and the temperature distribution and uniformly spaced thermal flux lines are also shown in the inset figure.

configuration obtained by MLP and the PSO algorithm have a higher symmetry and regularity. Moreover, some fuzzy local structural characteristics of the optimal configuration shown in previous studies have been reproduced, extended, and further optimized here.<sup>34,35</sup> In addition, we compare the performance of MLP and other artificial predictive models, such as mean local angle of thermal flux (MLATF),<sup>55,56</sup> mean length of thermal flux line (MLTFL), and artificial predictive model,<sup>35</sup> as shown in Figs. 1(h), S8, and S9. The automatic search method based on a combination of MLP and PSO optimization will be more accurate and extendable in the designing of porous thermal metamaterials (detailed discussions in the [supplementary material](#) Method S4).

To verify our theoretical predictions, a system based on the steady-state thermal flux method is built up in a vacuum chamber, where the pressure lower than  $10^{-6}$  mbar during measurement is provided to avoid the possible effects of thermal convection, thermal radiation, etc., and the detailed setup is shown in Figs. 3(a) and 3(b). The copper substrate and cooper sheet are served as the heater and the sink, respectively. The temperature gradient and thermal flux on the sample are obtained by two thermal sensors. The front and side view of the measurement system are shown in Figs. S10(a) and S10(b), respectively. The prepared porous materials are shown in Fig. S10(c),

and the details of the experimental measurements are shown in Method S5.

In the experiment, the polyimide thermal tapes with a relatively low thermal conductivity ( $0.1\text{--}0.35\text{ W m}^{-1}\text{ K}^{-1}$ )<sup>157,58</sup> are used to improve the thermal contact between the thermal flux sensors and the sample. As shown in Fig. 3(c), the ETC of the whole system shows an apparently abnormal enhancement and normal reduction, verifying our theoretical prediction. In order to obtain the intrinsic thermal transport properties, the temperature difference cross-matching method (the details in the [supplementary material](#) Method S6) is used to eliminate the possible effect from the interface thermal resistance (ITR), thermal tape as well as the measurement system. Here, we define these effects as the effective ITR ( $R_{\text{eff},i}$ ) as follows:

$$R_{\text{eff},i} = R_{\text{total thermal tap}} + 2R_{\text{thermal flux sensor}} + R_{\text{total interface}}, \quad (6)$$

where  $R_{\text{total thermal tap}}$ ,  $R_{\text{thermal flux sensor}}$ , and  $R_{\text{total interface}}$  represent the resistance of the total thermal tap, thermal flux sensor, and the total interface, respectively.

Moreover, an identical structure, including the thermal tape, the thermal flow direction regulator, the cooper heater, and the copper sheet, is established by using the FEM to achieve the temperature difference cross-matching method. In Fig. 3(d), it is apparently observed

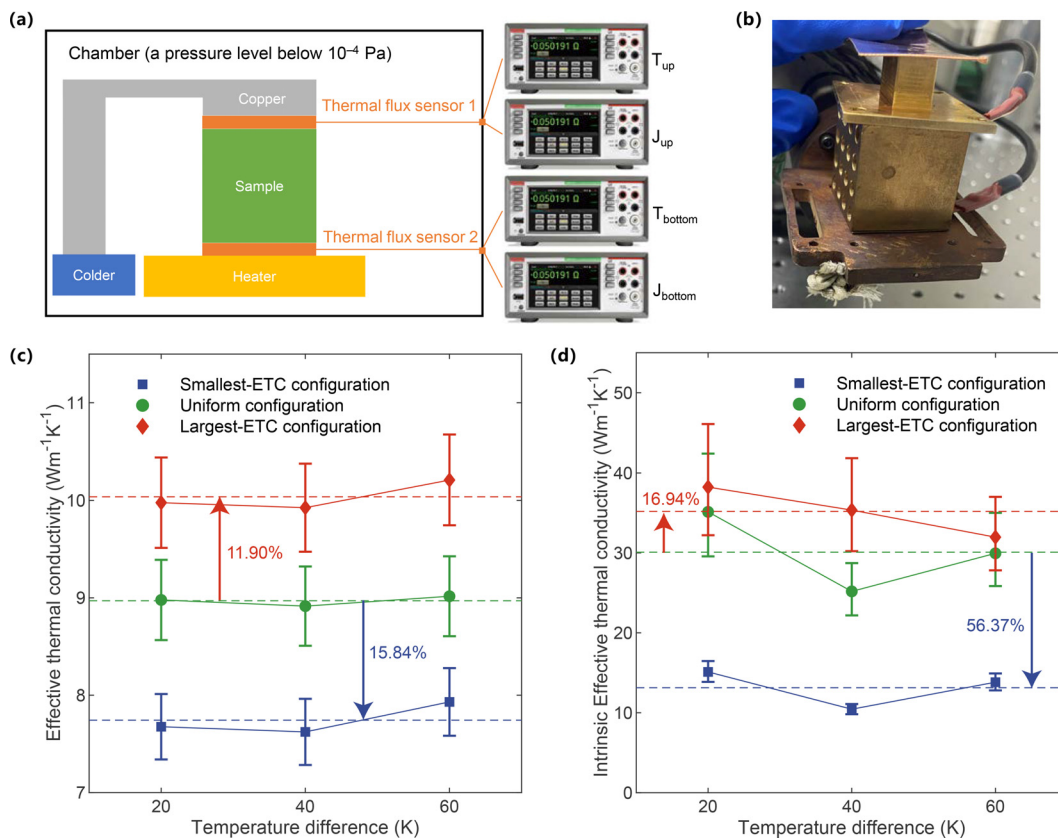


**FIG. 3.** The schematic diagram and the result of experimentally measuring the optimal disordered configuration. (a) A schematic diagram of experimentally measuring the ETC of the optimal disordered configuration. (b) The front view of the experimental measurement system. (c) and (d) The experimental measurement results of the ETC and the intrinsic ETC of the largest-ETC configuration (red diamond), uniform arrangement configuration (green circle), and smallest-ETC configuration (blue square) under different temperature differences. The dotted line gives the mean of the ETC and the intrinsic ETC in the different temperature difference cases.



that once considering the  $R_{\text{eff},i}$ , the intrinsic ETC is well in agreement with the theoretical prediction, and a more obviously abnormal enhancement and a normal reduction in intrinsic ETC have been observed. The relative change factor  $\mu$  after considering  $R_{\text{eff},i}$  is shown in Fig. S11(e), which is well consistent with the theoretical prediction as well. The structure with an anisotropy ratio  $\gamma$  as high as 1.62, as predicated by our calculation, is verified in the experiment performed in our study.

The mechanism behind the abnormal enhancement and the normal reduction in the intrinsic ETC is further discussed here. In Eqs. (S6) and (S7),  $\nabla T(x, y)$  gives the thermal flux direction of the entire material. Similar to the electric field line, each thermal flux line is a separate contribution to the entire material, and the overall ETC is summation of all individual thermal flux lines. The mathematical form is as follows:

$$\frac{1}{R_e} = \sum_i \frac{1}{R_i} = \sum_i \frac{S_i}{\rho l_i}. \quad (7)$$

In Eq. (7),  $i$  represents  $i$ th separate thermal flux line, and  $l_i$  and  $S_i$  represent the length and cross-sectional area of the  $i$ th thermal flux line, respectively. If the thermal flux lines in the porous material are straight and slightly curved, the local angle of thermal flux would decrease, leading to a larger ETC. In Fig. S8 for the smallest-ETC configuration, there are some large bright spots and bright bands along the local angle of thermal flux, meaning a significantly larger local angle of thermal flux than other configurations as well as a smaller ETC. In the macroscopic systems, the abnormal enhancement in thermal

conductivity could not arise from the wave-like behavior of phonons<sup>34</sup> but from the particle-like behavior of phonons,<sup>9,35</sup> which is closely related to the special geometric factor.

Furthermore, considering the fact that large number of pores and even complex porous structures are typically employed in the practical applications, the porous configurations with more periodic units, different number of layers, and blocks are constructed as shown in Fig. S12. As the block becomes larger, the structural anisotropy ratio also increases rapidly, which could increase to 40 when the number of units in the block is 10 and the structure ratio is about 0.5, as shown in Fig. 4(a). Here, the structure ratio is defined as the number of layers divided by the maximum number of layers, and the corresponding normalized thermal flux is shown in Fig. S13(a). Such a high structural anisotropic ratio would be beneficial to improve the overall anisotropic ratio, even though the material itself has a lattice anisotropy. The overall anisotropic ratio, including the combined effects of the structural anisotropic ratio and material anisotropic ratio, could be significantly improved once considering the optimal structure ratio for each block as shown in Figs. 4(b) and S13(b). It is worth noting that the structure anisotropy dominates in the overall anisotropy, as shown in Fig. S13(c). Therefore, it is desirable and useful to use this high structural anisotropy for thermal control. In Fig. 4(c), an example of using a porous structure with a highly thermal anisotropic ratio to heat an NNU-shaped region is shown, which includes various forms of management of thermal fluxes. More importantly, the structural anisotropy of such porous structures does not change with the scaling of the smallest structural unit [Fig. S13(d)], so the design of such highly

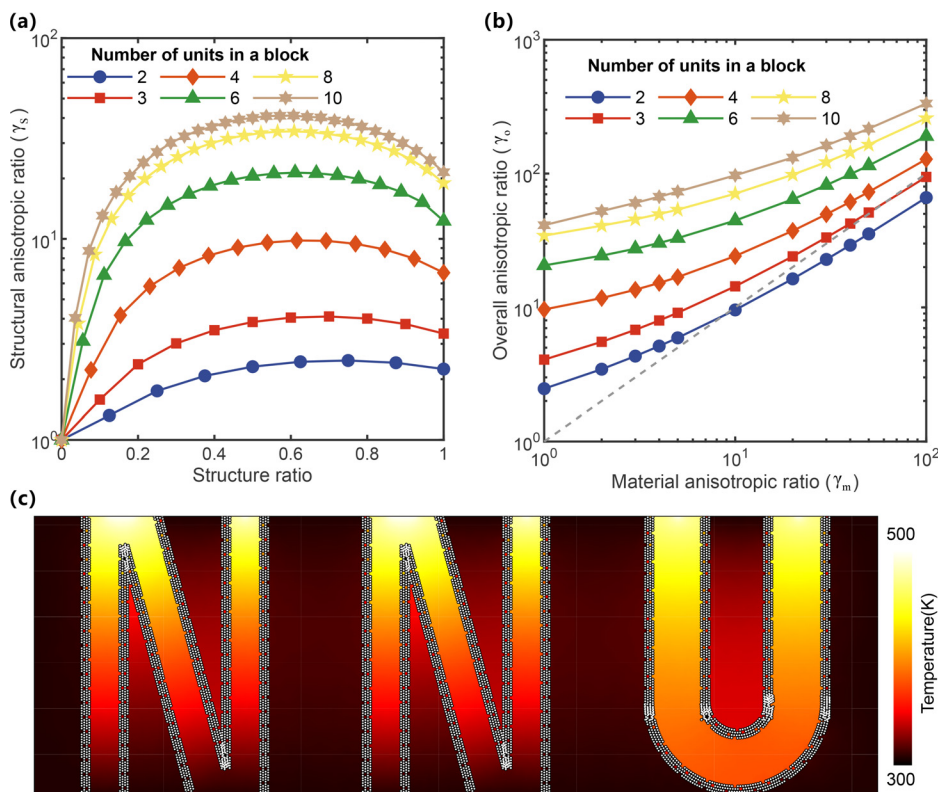


**FIG. 4.** Anisotropy and application of porous materials with the extended block. (a) The structural anisotropic ratio as a function of structure ratio for different number of units in a block. (b) The overall anisotropic ratio as a function of material anisotropic ratio for different number of units in a block. Here, the gray dashed line indicates that the material anisotropy is equal to the overall anisotropy. (c) An application example of using high-anisotropic porous materials to redirect the thermal flux and an artificially NNU is designed.

anisotropic porous materials would be flexible and has potential applications in thermal control and thermal management.

In summary, we study the effect of disorder on the ETC of porous materials. An optimal disorder configuration with the largest abnormal enhancement in ETC of the porous material is shown at the macroscopic limit and at room temperature, and a steady-state thermal flux method measurement system is used to verify these theoretical calculations results. According to our study, the abnormal enhancement in ETC does not come from the contribution of the coherent phonons, while is closely related to the geometric arrangement of the pores in the configuration, and even exists in the system with a high interface thermal resistance. The systematic optimization method we proposed in this work can be extended to the system with different shapes of pores and different porosity. Moreover, a combination of a series of basic units in the block will lead to an ultra-high structural anisotropy to obtain the function of redirecting, splitting, and turning the thermal flux, which will be of great significance for advancing the application of porous metamaterials to achieve the flexible and high-performance thermal management and control.

See the [supplementary material](#) for the details.

This work was supported by the National Natural Science Foundation of China (Grants Nos. 11975125, 11890703, and 12204244) and the Natural Science Foundation of Jiangsu Province (Grant No. BK20210556). Z.Y.S. acknowledges support from the Jiangsu Specially-Appointed Professor Program. Y.Y. acknowledges support from the Postgraduate Research & Practice Innovation Program of Jiangsu Province (Grant No. KYCX22 1539).

## AUTHOR DECLARATIONS

### Conflict of Interest

The authors have no conflicts to disclose.

## Author Contributions

**Yu Yang:** Conceptualization (equal); Data curation (equal); Formal analysis (equal); Writing – original draft (equal); Writing – review & editing (equal). **Yunshan Zhao:** Conceptualization (equal); Data curation (equal); Funding acquisition (equal); Project administration (equal); Resources (equal); Supervision (equal); Validation (equal); Writing – original draft (equal); Writing – review & editing (equal). **Lifa Zhang:** Conceptualization (equal); Data curation (equal); Investigation (equal); Resources (equal); Supervision (equal); Validation (equal); Writing – original draft (equal); Writing – review & editing (equal).

## DATA AVAILABILITY

The data that support the findings of this study are available within the article and its [supplementary material](#).

## REFERENCES

- M. M. Waldrop, *Nature* **530**, 144 (2016).
- Q. Wang, B. Jiang, B. Li, and Y. Yan, *Renewable Sustainable Energy Rev.* **64**, 106 (2016).
- Z. Liu, *Nature* **500**, 143 (2013).
- Y. Li, W. Li, T. Han, X. Zheng, J. Li, and B. Li, *Nat. Rev. Mater.* **6**, 488 (2021).
- S. R. Sklan and B. Li, *Nat. Sci. Rev.* **5**, 138 (2018).
- N. Li, J. Ren, L. Wang, G. Zhang, P. Hänggi, and B. Li, *Rev. Mod. Phys.* **84**, 1045 (2012).
- M. N. Luckyanova, J. Garg, K. Esfarjani, A. Jandl, M. T. Bulsara, A. J. Schmidt, A. J. Minnich, S. Chen, M. S. Dresselhaus, Z. Ren, E. A. Fitzgerald, and C. Gang, *Science* **338**, 936 (2012).
- J. K. Yu, S. Mitrovic, D. Tham, J. Varghes, and J. R. Heath, *Nat. Nanotechnol.* **5**, 718 (2010).
- J. Chen, D. Pan, X. Wang, N. Yang, J. Zhu, S. A. Yang, and G. Zhang, *Nature Mater.* **14**, 667–674 (2015).
- B. L. Davis and M. I. Hussein, *Phys. Rev. Lett.* **112**, 055505 (2014).
- B. Li, L. Wang, and G. Casati, *Phys. Rev. Lett.* **93**, 184301 (2004).
- B. Li, L. Wang, and G. Casati, *Appl. Phys. Lett.* **88**, 143501 (2006).
- C. Z. Fan, Y. Gao, and J. P. Huang, *Appl. Phys. Lett.* **92**, 251907 (2008).
- R. Schittny, M. Kadic, S. Guenneau, and M. Wegener, *Phys. Rev. Lett.* **110**, 195901 (2013).
- S. Narayana and Y. Sato, *Phys. Rev. Lett.* **108**, 214303 (2012).
- T. Vasileiadis, J. Varghese, V. Babacic, J. Gomis-Bresco, D. N. Urrios, and B. Graczykowski, *J. Appl. Phys.* **129**, 160901 (2021).
- M. Maldovan, *Phys. Rev. Lett.* **110**, 025902 (2013).
- M. Maldovan, *Nature Nano.* **5**, 718–721 (2010).
- D. Song and G. Chen, *Appl. Phys. Lett.* **84**, 687 (2004).
- P. E. Hopkins, C. M. Reinke, M. F. Su, R. H. Olsson III, E. A. Shaner, Z. C. Leseman, J. R. Serrano, L. M. Phinney, and I. El-kady, *Nano Lett.* **11**, 107 (2011).
- L. Yang, N. Yang, and B. Li, *Nano Lett.* **14**, 1734 (2014).
- S. Alaie, D. F. Goettler, M. Su, Z. C. Leseman, C. M. Reinke, and I. El-Kady, *Nat. Commun.* **6**, 7228 (2015).
- T. Feng and X. Ruan, *Carbon* **101**, 107 (2016).
- Y. Zhao, L. Yang, L. Kong, M. H. Nai, D. Liu, J. Wu, Y. Liu, S. Y. Chiam, W. K. Chim, C. T. Lim, B. Li, J. T. L. Thong, and K. Hippalgaonkar, *Adv. Funct. Mater.* **27**, 1702824 (2017).
- J. H. Lee, G. A. Galli, and J. C. Grossman, *Nano Lett.* **8**, 3750 (2008).
- J. Tang, H. T. Wang, D. H. Lee, M. Fardy, Z. Huo, T. P. Russell, and P. Yang, *Nano Lett.* **10**, 4279 (2010).
- R. Anufriev, A. Ramiere, J. Maire, and M. Nomura, *Nat. Commun.* **8**, 15505 (2017).
- M. Kasprzak, M. Sledzinska, K. Zaleski, I. Iatsunskyi, F. Alzina, S. Volz, C. M. S. Torres, and B. Graczykowski, *Nano Energy* **78**, 105261 (2020).
- M. R. Wagner, B. Graczykowski, J. S. Reparaz, A. E. Sachat, M. Sledzinska, F. Alzina, and C. M. S. Torres, *Nano Lett.* **16**, 5661 (2016).
- J. Oh, H. Yoo, J. Choi, J. Y. Kim, D. S. Lee, M. J. Kim, J. C. Lee, W. N. Kim, J. C. Grossman, J. H. Park, S. S. Lee, H. Kim, and J. G. Son, *Nano Energy* **35**, 26 (2017).
- S. Hu, Z. Zhang, P. Jiang, J. Chen, S. Volz, M. Nomura, and B. Li, *J. Phys. Chem. Lett.* **9**, 3959 (2018).
- S. Hu, Z. Zhang, P. Jiang, W. Ren, C. Yu, J. Shiomi, and J. Chen, *Nanoscale* **11**, 11839 (2019).
- M. Sledzinska, B. Graczykowski, F. Alzina, U. Melia, K. Termentzidis, D. Lacroix, and C. M. S. Torres, *Nanotechnology* **30**, 265401 (2019).
- J. Maire, R. Anufriev, R. Yanagisawa, A. Ramiere, S. Volz, and M. Nomura, *Sci. Adv.* **3**, e1700027 (2017).
- H. Wei, H. Bao, and X. Ruan, *Nano Energy* **71**, 104619 (2020).
- Y. F. Huang, Z. G. Wang, H. M. Yin, J. Z. Xu, Y. Chen, J. Lei, L. Zhu, F. Gong, and Z. M. Li, *ACS Appl. Nano Mater.* **1**, 3312 (2018).
- Z. G. Wang, W. Liu, Y. H. Liu, Y. Ren, Y. P. Li, L. Zhou, J. Z. Xu, J. Lei, and Z. M. Li, *Composites, Part B* **180**, 107569 (2020).
- I. I. Smalyukh, *Adv. Mater.* **33**, 2001228 (2021).
- R. Ramprasad, R. Batra, G. Pilania, A. Mannodi-Kanakkithodi, and C. Kim, *npj Comput. Mater.* **3**, 54 (2017).
- H. Zhang, K. Hippalgaonkar, T. Buonassisi, O. M. Løvvik, E. Sagvolden, and D. Ding, *ES Energy Environ.* **2**, 1–8 (2018).
- X. Wan, W. Feng, Y. Wang, H. Wang, X. Zhang, C. Deng, and N. Yang, *Nano Lett.* **19**, 3387 (2019).
- T. Zhan, L. Fang, and Y. Xu, *Sci. Rep.* **7**, 7109 (2017).
- Y. J. Wu, L. Fang, and Y. Xu, *npj Comput. Mater.* **5**, 56 (2019).

- <sup>44</sup>H. Wei, S. Zhao, Q. Rong, and H. Bao, *Int. J. Heat Mass Transfer* **127**, 908 (2018).
- <sup>45</sup>Q. Rong, H. Wei, X. Huang, and H. Bao, *Compos. Sci. Technol.* **184**, 107861 (2019).
- <sup>46</sup>H. Miyazaki, T. Tamura, M. Mikami, K. Watanabe, N. Ide, O. M. Ozkendir, and Y. Nishino, *Sci. Rep.* **11**, 13410 (2021).
- <sup>47</sup>Y. Saito, K. Shin, K. Terayama, S. Desai, M. Onga, Y. Nakagawa, Y. M. Itahashi, Y. Iwasa, M. Yamada, and K. Tsuda, *NPJ Comput. Mater.* **5**, 124 (2019).
- <sup>48</sup>R. Hu, S. Iwamoto, L. Feng, S. Ju, S. Hu, M. Ohnishi, N. Nagai, K. Hirakawa, and J. Shiomi, *Phys. Rev. X* **10**, 021050 (2020).
- <sup>49</sup>P. R. Chowdhury, C. Reynolds, A. Garrett, T. Feng, S. P. Adiga, and X. Ruan, *Nano Energy* **69**, 104428 (2020).
- <sup>50</sup>J. Kennedy and R. Eberhart, in Proceedings of ICNN'95—International Conference on Neural Networks, 1995, Vol. 4.
- <sup>51</sup>K. E. Parsopoulos and M. N. Vrahatis, *Nat. Comput.* **1**, 235 (2002).
- <sup>52</sup>M. Weiel, M. Götz, A. Klein, D. Coquelin, R. Floca, and A. Schug, *Nat. Mach. Intell.* **3**, 727 (2021).
- <sup>53</sup>M. S. Alvarez-Alvarado, F. E. Alban-Chacón, E. A. Lamilla-Rubio, C. D. Rodríguez-Gallegos, and W. Velásquez, *Sci. Rep.* **11**, 11655 (2021).
- <sup>54</sup>Y. Xiao and Q. Hao, *Int. J. Heat Mass Transfer* **170**, 120944 (2021).
- <sup>55</sup>G. H. Tang, C. Bi, and B. Fu, *J. Appl. Phys.* **114**, 184302 (2013).
- <sup>56</sup>B. Fu, G. H. Tang, and C. Bi, *J. Appl. Phys.* **116**, 124310 (2014).
- <sup>57</sup>T. L. Li and S. L. C. Hsu, *J. Phys. Chem. B* **114**, 6825 (2010).
- <sup>58</sup>T. Wang, M. Wang, L. Fu, Z. Duan, Y. Chen, X. Hou, Y. Wu, S. Li, L. Guo, R. Kang, N. Jiang, and J. Yu, *Sci. Rep.* **8**, 1557 (2018).

# Machine learning boosting the discovery of porous metamaterials with an abnormal thermal transport property

Yu Yang<sup>1</sup>, Yunshan Zhao<sup>1,\*</sup>, Lifa Zhang<sup>1,\*</sup>

<sup>1</sup> Phonon Engineering Research Center of Jiangsu Province, Center for Quantum Transport and Thermal Energy Science, Institute of Physics Frontiers and Interdisciplinary Sciences, School of Physics and Technology, Nanjing Normal University, Nanjing 210023, China

\*Corresponding authors. E-mails: phyzys@njnu.edu.cn; phyzlf@njnu.edu.cn

## This PDF file includes:

Section S1 to Section S4

Figure S1 to Figure S16

Method S1 to Method S6

Table S1 to Table S2



19	This PDF file includes:
20	<b><i>Section S1 Establishment, test and application of the multi-layer perceptron (MLP)</i></b>
21	Method S1 Finite Element Method
22	Method S2 Multi-layer perceptron
23	Method S3 Particle swarm optimization algorithm
24	Method S4 mean local angle of thermal flux (MLATF) and mean length of thermal flux line (MLTFL)
25	Figure S1 The effective thermal conductivity of random configuration in different degrees of disorder
26	Figure S2 Schematic diagram of the multi-layer perceptron
27	Figure S3 The training process of the multi-layer perceptron
28	Figure S4 Regression analysis of the accuracy of multi-layer perceptron
29	Figure S5 Absolute error analysis of multi-layer perceptron
30	Figure S6 Process diagram of particle swarm optimization algorithm
31	Figure S7 Anisotropy in disordered configuration under different degrees of disorder
32	Figure S8 Local angle of thermal flux of different configurations
33	Figure S9 Regression analysis of the accuracy of MLATF method and MLTFL method
34	<b><i>Section S2 Analysis and modifide the primitive effective thermal conductivity</i></b>
35	Method S5 Sample fabrication and measurement details
36	Method S6 The temperature difference cross-matching method
37	Figure S10 Experimental measurement system
38	Figure S11 Experimental measurement with considering the effect of interface thermal resistance
39	Table S1 Effective interface thermal conductivity
40	<b><i>Section S3 Highly anisotropic porous structure with extended blocks</i></b>
41	Figure S12 Schematic illustration of the highly anisotropic porous structure of the extended block used in
42	FEM calculation
43	Figure S13 Anisotropy properties of porous materials with extended block
44	<b><i>Section S4 What did the multi-layer perceptron learn?</i></b>
45	Figure S14 The normalized $MIV_{45}$ between the hidden layer 4 and the output layer 5
46	Figure S15 The features of the effective thermal conductivity learned by the multi-layer perceptron learn
47	Figure S16 The schematic diagram of features of the largest thermal conductivity configuration learned
48	by the multi-layer perceptron learn after PCA processing



## *Section S1 Establishment, test and application of the multi-layer perceptron learn*

Because of its higher accuracy, the multi-layer perceptron (MLP) has been selected as the predictive model between the generated configuration and its effective thermal conductivity (ETC). Before training MLP, we investigate 2000 randomly generated configurations in different degrees of disorder, and their ETC are shown in Fig. S1. It is very easy to find the configurations with abnormal enhancement in ETC, especially for the high disorder case. Then, 55,000 initial random configurations are used as training data to train a four-layer perceptron, and the framework of the MLP is shown in Fig. S2. A highly accurate Levenberg-Marquardt algorithm is used to train the MLP, and the gradient function and the cumulative failures of the validation set are shown in Fig. S3. The correlation coefficient  $R$  and the mean square error  $MSE$  is 0.9856 and  $1.9 \times 10^{-4}$ , which shows that the MLP can accurately describe the relationship between the configuration parameters and ETC. In particular, Figure S4 shows that the training sets, the validation set and the test set all have consistent high accuracy, implying that while maintaining high accuracy, over-fitting does not appear in high-performance MLP. Simultaneously, the absolute error between the predicted- and accurate- ETC is given in Fig. S5. The absolute error has a good Gaussian distribution, and the full width at half maxima is less than 5% of the maxima. In addition, we discussed the savings of MLPS on computing consumption. ETC of 100 random configurations were calculated by FEM method and MLP prediction model respectively. The FEM method took 657.5765 seconds, while the MLP only took 1.3862 seconds, saving 99.79% of the calculation time, which provides nearly 500 times acceleration for finding the optimal configuration later.

These tests prove that MLP has high accuracy and provide great convenience to find the optimal disordered configuration. Because of its advantages in dealing with global optimization at high degree of freedom, we chose the particle swarm optimization (PSO) algorithm to handle this problem. The particle distribution at each optimization step in a typical optimization process is given in Fig. S6, and almost all particles have reached the vicinity of the optimal disordered configuration at about 30 steps. After that, we compare and prove that the anisotropy of the optimal disordered configuration predicted by PSO is very consistent with

the results given by the finite element method, and the result is shown in Fig. S7. Then, local angle of thermal flux of different configurations is shown in Fig. S8, and is used to explain the difference in ETC of different configurations. Finally, in addition to using MLP, we also use various predictive models proposed in the past for comparison and test, such as: mean local angle of thermal flux method (MLATF) and mean length of thermal flux line method (MLTFL). The regression analysis of the MLATF method and the MLTFL method is shown in Fig. S9. The broadening of the scattered dots is obviously larger than that of the MLP, which also proves that the MLP has a great advantage in accuracy.

## Method S1 Finite Element Method

COMSOL Multiphysics Simulation Software is utilized to conduct structural element analysis for porous materials. A large number of disordered configurations are randomly generated, and their random uniformity is tested. A steady-state solid heat transfer module is used to calculate the effective thermal conductivity of these randomly generated disordered configurations. In the calculation, for simplicity, we use a two-dimensional model. For all boundaries that do not contain heat source, we set them as thermal insulation boundaries, which satisfy the following equation:

$$-\mathbf{n} \cdot \mathbf{q} = 0. \quad (\text{S1})$$

Here,  $\mathbf{n}$  and  $\mathbf{q}$  represent the normal vector of the boundary and the direction vector of thermal flux, respectively. The surface is divided into extremely fine triangular meshes to more accurately calculate the disordered porous structure with tangent circular dimer structure. A domain probe is used to calculate the average thermal flux  $J$  in the direction of the external thermal temperature difference. The effective thermal conductivity  $\kappa_e$  can be calculated by Fourier's law, as follows:

$$\kappa_e = \frac{J}{\Delta T}. \quad (\text{S2})$$

## Method S2 Multi-layer perceptron (MLP)

The displacement data of 32 dimensions were normalized as input data, and the corresponding ETC calculated by FEM was normalized as a single output data. A total of 55,000 disordered configurations are

generated randomly, which will be divided into training set, validation set and test set with a ratio of 0.7:0.15:0.15. In this paper, we use nntaintool library based on Matlab R2021a to build MLP to realize prediction of ETC. At the beginning, we need to find the optimal structure of the MLP to achieve the best regression function. Since the input data have 32 deminsion, the number of neurons in each layer is selected as an integer multiple of 2, and the traversal search is carried out to obtain the optimal structure of MLP. Part of the optimization results are given in the Table S2.

Finally, a fully connected MLP with 5 layers of one input layer, one output layer and 3 hidden layers are used as the basis of the predictive model. Each neuron in MLP is connected to every neuron in the next layer, while without non-adjacent layer connections and intra-layer connections. The input data is perceived and learned layer by layer in the MLP, which can be described by two parameters, weight, and bias. In this work, we denote the weight from the  $i$ -th neuron in the  $(m - 1)$ -th layer to the  $j$ -th neuron in the  $m$ -th layer as  $w_{ji}^m$ , the bias of the  $j$ -th neuron in the  $m$ -th layer as  $b_j^m$  and the output of the  $j$ -th neuron in the  $m$ -th layer as  $a_j^m$ . The nonlinear activation function is used to connect adjacent layers, and its mathematical form is as follows:

$$a_j^m = f_a(\sum_i w_{ji}^m a_i^{m-1} + b_j^m). \quad (S3)$$

The tansig function is used as the nonlinear activation function for the hidden layer, and the purelin function is used as the activation function for the output layer. The specific network settings are given in detail in Fig. S2. We train the MLP using the Levenberg-Marquardt training algorithm and the mean square error as the cost function to estimate the performance of the MLP. In the training, the max epoch is set as 10000 and the goal performance is set as  $10^{-5}$ . The MSE of the validation set does not increase for 100 consecutive steps as the end point of training to prevent the occurrence of over-fitting. At the end of training, the test set has a fairly high correlation coefficient close to 0.99, which is slightly higher than that of the validation set and test set.

### **Method S3 Particle swarm optimization (PSO) algorithm**



The particle swarm optimization algorithm is a computational-intelligence technique that is inspired by the foraging of biological population to handle with complex global optimization problem. The PSO algorithm considers a swarm of particles moving in the parameter space, and the position of each particle corresponds to a point in the parameter space. In this work, 300 randomly generated initial particles as the initial population are expected to find the optimal disordered configuration in a fairly high 32-dimensional parameter space. All particles will jump in the parameter space to generate the next generation. For any individual particle  $i$ , we make it move as follows:

$$\mathbf{x}_i^{new} = \begin{cases} \mathbf{x}_i^{old} + \mathbf{v}_i^{new}, & \mathbf{x}_i^{old} + \mathbf{v}_i^{new} < \mathbf{x}_i^{max} \\ \mathbf{x}_i^{max}, & \mathbf{x}_i^{old} + \mathbf{v}_i^{new} \geq \mathbf{x}_i^{max} \end{cases} \quad (S4)$$

In above equation,  $\mathbf{x}$  represents the position of the particle in the parameter space, and  $\mathbf{v}$  represents the displacement moved by this generation, which is usually called velocity. In the evolution process of generations, particles remember their personal best position and the global best position in the entire population. These memories act as attractors in the parameter space and help the particles converge to find the global optimal location. Therefore, the velocity include the memory component of the current personal best position and the social component of the best global position in the population, and the mathematical form of velocity is as follows:

$$\mathbf{v}_i^{new} = \omega \mathbf{v}_i^{old} + c_1 \gamma_1 (\mathbf{x}_i^{pb} - \mathbf{x}_i^{old}) + c_2 \gamma_2 (\mathbf{x}_i^{gb} - \mathbf{x}_i^{old}), \quad (S5)$$

where the inertia coefficient  $\omega$  and the acceleration coefficients  $c_1$  and  $c_2$  set as 0.8, 1.49445, and 1.49445, respectively. The variables  $\mathbf{x}_i^{pb}$  and  $\mathbf{x}_i^{gb}$  represent the personal best position of particles  $i$  and the global best position of entire population, respectively. Similarly, if the speed exceeds the speed threshold  $\mathbf{v}_i^{max} = 0.1 \mathbf{x}_i^{max}$ , it will be cut off. Eventually, multiple mechanisms such as velocity clamping, inertia weight or contraction will gradually converge the population. Occasionally, for the population to converge to a local maximum, we continue to search through annealing algorithm processing, and continue to cycle this process. After multiple search, the optimal disordered configuration appears once the population is stable in a certain position.

#### Method S4 mean local angle of thermal flux (MLATF) and mean length of thermal flux line (MLTFL)

In this work, in addition to using MLP, we also use other predictive models for comparison, such as: mean local angle of thermal flux (MLATF) [1,2], mean length of thermal flux line (MLTFL), artificial predictive model [3], etc. The mean local angle of thermal flux and the mean length of thermal flux line is defined as follows:

$$\text{MLATF} = \frac{\oint_{\text{Non-porous area}} \cos^{-1}(\nabla T(x,y) \cdot \hat{x}) dx dy}{\oint_{\text{Non-porous area}} dx dy}, \quad (\text{S6})$$

$$\text{MLTFL} = \frac{\oint_{\text{Non-porous area}} \sqrt{1 + \tan^2(\cos^{-1}(\nabla T(x,y) \cdot \hat{x}))} dx dy}{a}, \quad (\text{S7})$$

where  $T(x, y)$  represents the temperature field in the non-porous area, and  $\hat{x}$  represents the unit vector in the  $x$  direction. In the actual calculation, we discretize the whole area into an  $800 \times 800$  grid area in order to simplify the calculation. The local angle of the thermal flux is shown in Fig. S8, where the uniform arrangement has four-degree rotational symmetry, similar to the treatment by Fu *et al.* [2]. Moreover, the regression analysis of the MLATF method and the MLTFL method is shown in Fig. S9. As shown in Fig. S9, the red scattered dots indicate that the configuration has the lowest 90% absolute error, similar to that in Fig. S4, while the broadening caused by the remaining 10% configuration is not as significant as Fig. S4, implying that the accuracy of these two methods are lower than the MLP. We use these two predictive models to evaluate the configurations in the PSO optimization process. Basically, the MLATF method has a similar function, while its accuracy is relatively poor, and the MLTFL loses its effectiveness in the largest-ETC optimization process. In order to describe their accuracy quantitatively, we calculate the correlation coefficients  $R$  with 2000 data as shown in Fig. S1 ( $\delta_m = 0.2$ ), and the result is shown in Fig. 1h. By using the MLP, the correlation coefficient  $R$  is basically close to 1, which is extremely higher than that of the previous methods like MLATF and MLTFL. Therefore, an automatic search design method based on a combination of MLP and PSO optimization is useful in designing anisotropic porous thermal metamaterials.

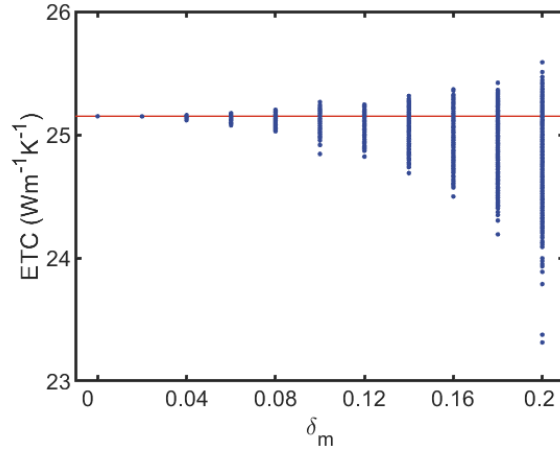


**Figure S1.** The effective thermal conductivity of random configuration in different degrees of disorder. We generate uniformly 2000 random disordered configurations in different degrees of disorder, and investigate their ETC by using the FEM. Under the high degree of disorder, the abnormal enhancement of ETC is significantly observed and account for about 8.2% of the total.

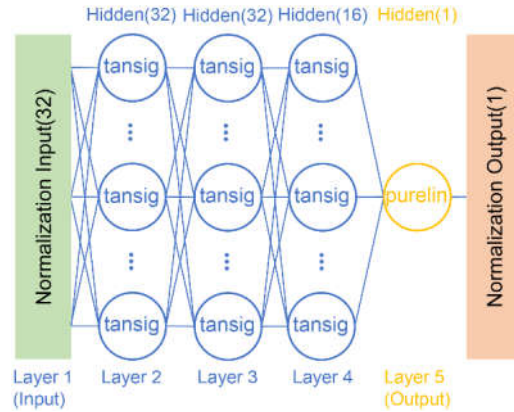
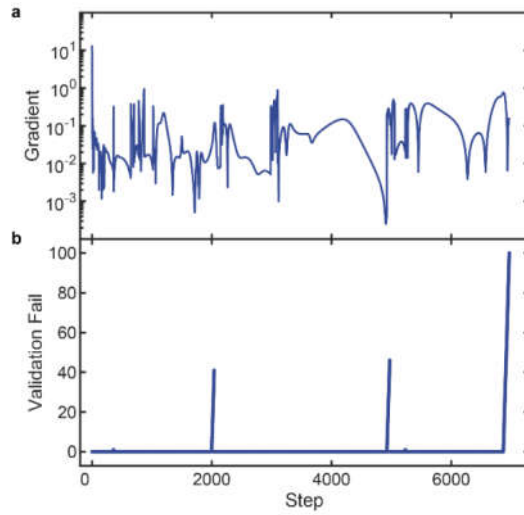
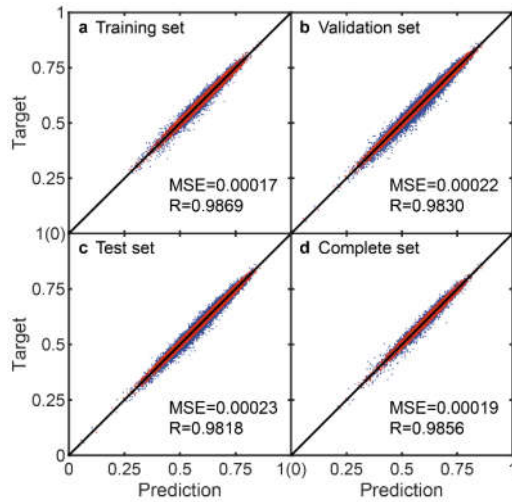


**Figure S2.** Schematic diagram of the MLP. We chose a 4-layer MLP as the carrier of the predictive model and the number of neurons in the hidden layer is 32, 32, 16, and 1. The first three hidden layers use the tansig activation function to learn the characteristics of the normalized input, and the fourth hidden layer uses the purelin function as the output layer to ensure the scalability of the MLP. The normalized input is composed of pore coordinates  $\mathbf{A} = (x_1, x_2, \dots, x_{16}, y_1, y_2, \dots, y_{16})$ .



179 **Figure S3.** The training process of the MLP. (a) The gradient is as a function of the training step. The  
 180 gradient here comes from the Levenberg-Marquardt algorithm, which shows that the rate of MLP training  
 181 has been relatively fast. (b) The number of consecutive failures in the validation set is as a function of the  
 182 training step. We can find that there are two large consecutive failures before the best predictive model is  
 183 obtained, but due to the large gradient in training, we quickly surpass those local optimal networks.



184 **Figure S4.** Regression analysis of the accuracy of MLP. Figures (a), (b), (c), and (d) respectively show the  
 185 regression analysis diagrams of the training set, validation set, test set and complete set. We calculate the  
 186 mean square error  $MSE$  and correlation coefficient  $R$  of the four sets, which prove that no overfitting

occurred while maintaining high accuracy. The red scattered dots indicate the configuration with the smallest 90% absolute error, which imply that the remaining 10% configuration brings greater broadening.

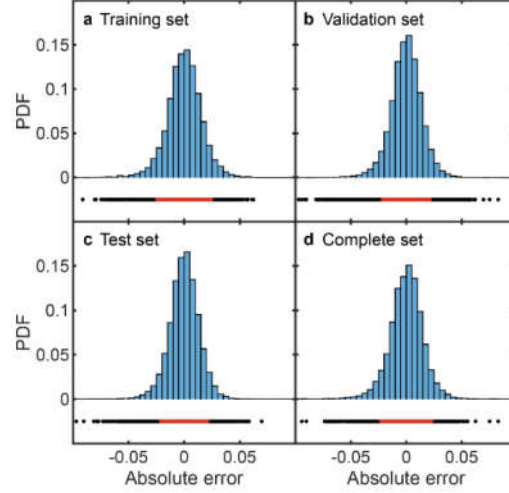


**Figure S5.** Absolute error analysis of MLP. Figures (a), (b), (c), and (d) respectively show the probability distribution function (PDF) of absolute error of the training set, validation set, test set and complete set. The absolute error has a good Gaussian distribution, and the full width at half maxima is less than 5% of the maximum value. The red scattered dots indicate the configuration with the smallest 90% absolute error, which imply that the remaining 10% configuration brings greater broadening.

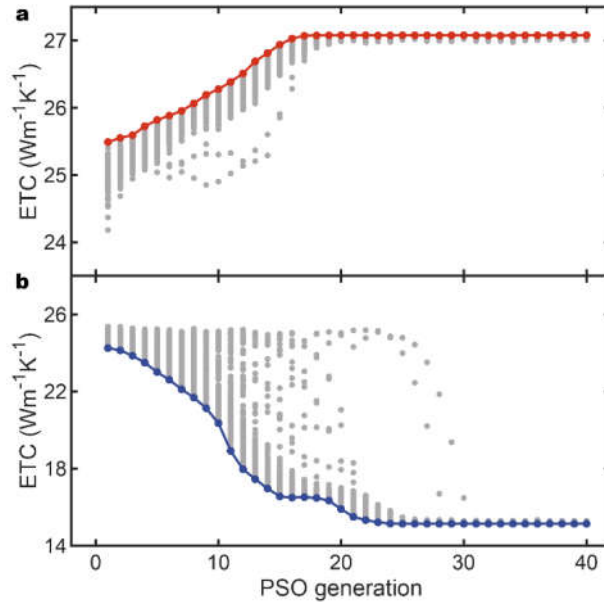




**Figure S6.** Process diagram of PSO algorithm. Figures (a) and (b) respectively show the particle distribution in each optimization step in a typical largest-ETC and smallest-ETC optimization process. At about 40 steps, almost all particles have reached the vicinity of the optimal disordered configuration.

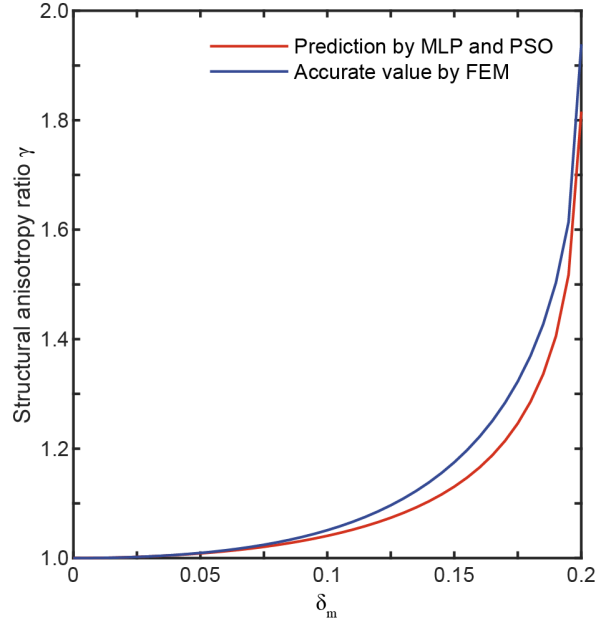
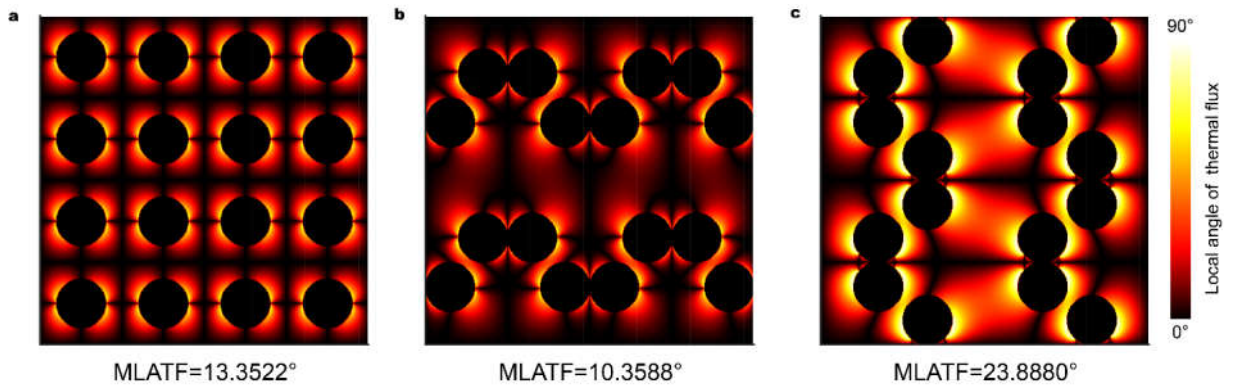


**Figure S7.** Anisotropy in disordered configuration under different degrees of disorder. The accurate anisotropy calculated by the finite element (blue line) and the anisotropy predicted by the MLP (red line)



are two functions of the degree of disorder.

**Figure S8.** Local angle of thermal flux of different configurations. Figure (a), (b) and (c) respectively show the map of local angle of thermal flux of the uniform configuration, the largest-ETC configuration, and the smallest-ETC configuration. The smallest-ETC configuration shows a local angle of thermal flux that is significantly larger than the other configurations.

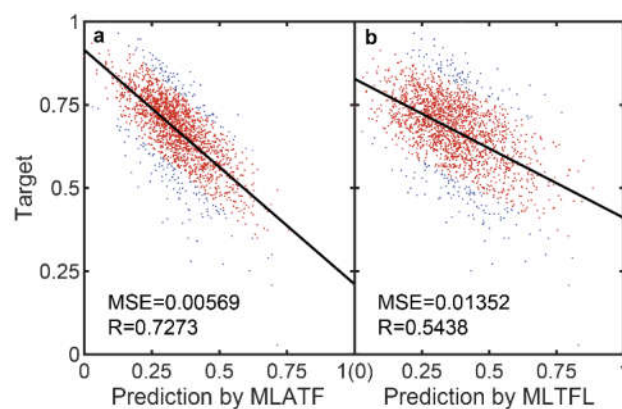


**Figure S9.** Regression analysis of the accuracy of MLATF method and MLTFL method. Figures (a) and (b) respectively show the regression analysis of the MLATF method and MLTFL method. We calculate the mean square error  $MSE$  and correlation coefficient  $R$  of these two methods. The red scattered dots indicate the configuration with the smallest 90% absolute error, but the broadening brought by the remaining 10% configuration here is not significant.

## ***Section S2 Analysis and modifide the primitive effective thermal conductivity***

In Figure S10a and S10b, we show the front and side view of the home-made system for measuring the thermal conductivity by using the steady-state thermal flux method. The porous materials we prepared are shown in Fig. S10c. The measurement result is shown in Fig. 3c, and the largest-effective thermal conductivity, the ETC of the uniform arrangement configuration, and the smallest-ETC are clearly shown in different colors. The largest-ETC is enhanced by 11.90% and the smallest-ETC is reduced by 15.84%, compaired to that of the uniform arrangement configuration. Although the ETC contains the influence of many factors such as interface thermal resistance, low thermal conductivity thermal tape, thermal radiation, etc., it still shows a very clear abnormal enhancement and normal reduction in ETC. In particular, the largest- and the smallest-ETC of the porous structures are also along the two directions of the same configuration with a structural anisotropy ratio of 2.

## **Method S5 Sample fabrication and measurement details**

16 pores are drilled on the surface of a phosphor copper cube with a width of 30mm to construct a three-dimensional measurement sample with an interface consistent with the FEM calculation. A simple system for measuring the effective thermal conductivity by using the steady-state thermal flux method is built in a vacuum chamber (CRYO INDUSTRIES), with a pressure lower than  $10^{-4}$ pa during measurement to reduce the effect of thermal convection. The copper substrate serves as a heater, and the copper sheet serves as a channel for connecting the room temperature thermostat. The temperature gradient and thermal flux on the sample are obtained by two thermal flux sensors. The front and side view of the experimental measurement system are shown in Fig. S10a and b, respectively, where a thermal flux direction regulator is used to adjust the thermal flux direction near the cube top surface. In order to ensure a good contact between the thermal flux sensor and the sample or the thermostat, the polyimide thermal tape is used to connect the joints. The thermal flux sensor we use has an error of less than 3%, a nominal sensitivity better than  $2.5 \mu\text{V} \cdot \text{Wm}^{-2}$ , and a response time of 0.3 s. The signal of the thermal flux sensor is recorded by the KEITHLEY

DMM6500 6 1/2 DIGIT MULTIMETER, which is programmed by Labview code. The effective thermal conductivity  $\kappa_e$  can be calculated by Fourier's law, as follows:

$$\kappa_e^{exp} = \frac{(J_{bottom} + J_{up})L}{2A(T_{bottom} - T_{up})}. \quad (S8)$$

Where  $L$  and  $A$  represent the side length and cross-sectional area of the cube, respectively.

#### Method S6 The temperature difference cross-matching method

Considering the large difference between the PETC and the theoretical prediction in smallest configuration, we quantitatively discuss the possible reasons of this difference. Combining Equation (3) and Equation (S2), the relative change factor can be expressed in the following form:

$$\mu = \frac{\kappa_s - \kappa_u}{\kappa_u} = \frac{\frac{J_s}{\Delta T_s} - \frac{J_u}{\Delta T_u}}{\frac{J_u}{\Delta T_u}} = 1 - \frac{J_u}{J_s} \frac{\Delta T_s}{\Delta T_u} = 1 - \frac{J_{real,u}}{J_{real,s}} \frac{\Delta T_{real,s} + \Delta T_{diff,s}}{\Delta T_{real,u} + \Delta T_{diff,u}}. \quad (S9)$$

where the subscripts  $s$  and  $u$  represent the smallest-ETC configuration and the uniform configuration, respectively. Considering the fact that the thermal flux  $J$  through any section is same under the non-equilibrium thermal steady state, so the thermal flux during measurement is not the origin of the difference above. Therefore, the difference should come from the inaccurate characterization of temperature measurement, and the measured temperature  $\Delta T_{s(u)}$  can be divided into two parts, the real temperature  $\Delta T_{real,s(u)}$  and the difference temperature  $\Delta T_{diff,s(u)}$ . Since the measured relative change factor is much smaller than the theoretical prediction, the difference temperature  $\Delta T_{diff,s(u)}$  should be larger than 0, considering that  $\Delta T_{diff,s}$  and  $\Delta T_{diff,u}$  are almost the same. So we confirm that these differences mainly come from the effect of the interface thermal resistance.

Subsequently, we use the temperature difference cross-matching method to determine the value of the interface thermal resistance in each measurement. At first, we construct a finite element structure identical to the experimental system, including thermal tape, thermal flow direction regulator, cooper heater, and copper sheet. After that, the temperature difference between two thermal sensors and the thermal flux in whole system with different interface thermal resistances are calculated and shown in Fig. S11c. The black

outline symbol in Fig. S11c indicates the results of temperature difference cross-matching, and the effective interface thermal conductivity in each measurement is shown in Table S1.

After considering the influence of effective interface thermal resistance, it is apparently observed that the ETC is significantly greater than ETC, and a more obvious abnormal enhancement and normal reduction in ETC has been observed. The relative change rate after considering the effective interface thermal resistance is shown in Fig. S11e, and is completely consistent with the theoretical prediction.

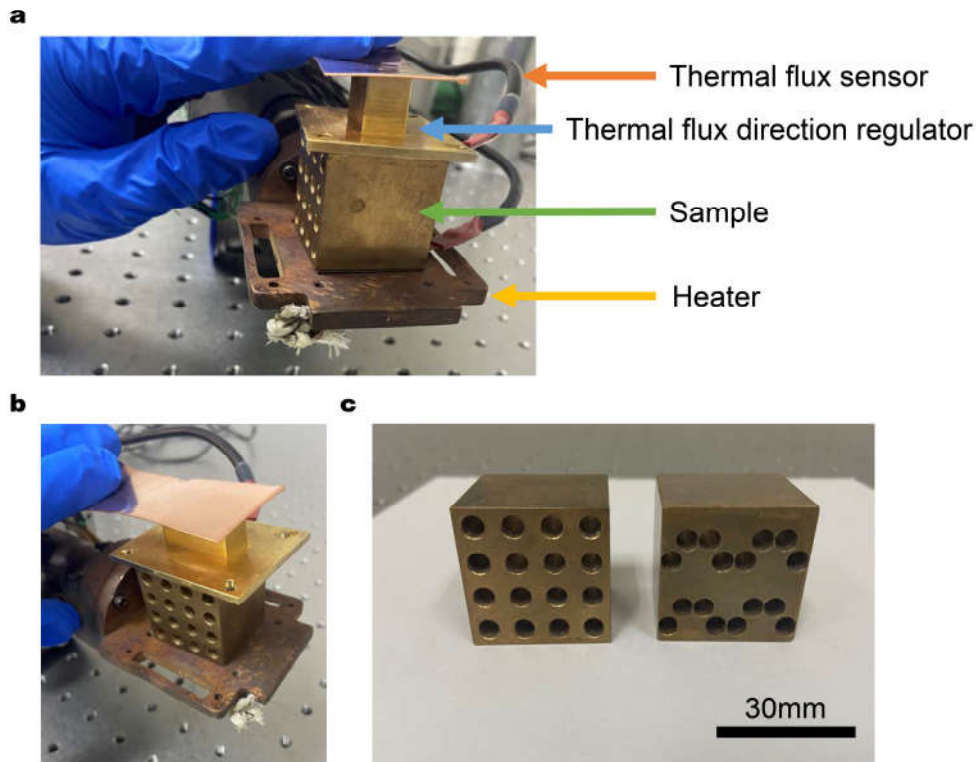


**Figure S10.** Experimental measurement system. Figure (a) and (b) show the front and side view of the experimental measurement system. Figure (c) shows the uniform configuration porous material and the largest- (or smallest-) ETC configuration porous material.



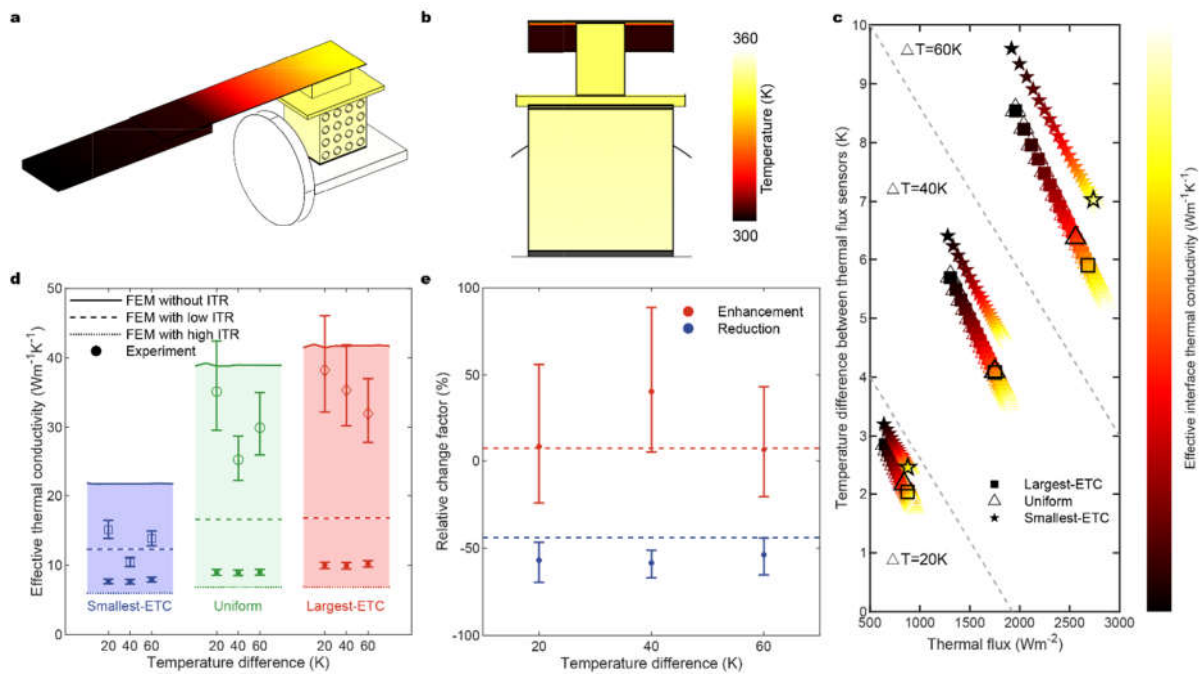


**Figure S11.** Experimental measurement with considering the effect of interface thermal resistance. Figure (a) and Figure (b) show the schematic diagram of the finite element simulation structure considering the influence of the interface thermal resistance. The thermal color shows the temperature distribution of the measurement system. It can be seen that the temperature difference on the sample after considering the interface thermal resistance is smaller and more consistent with the measured value. (c) The relationship between the sample thermal flux and the temperature difference between two the thermal flux sensors at different effective interface thermal conductivity at different external temperature differences. The black frame reflects the effective interface thermal conductivity value obtained from the temperature difference cross-matching. (d) Comparative analysis of experimental measurement results and FEM simulation results under different interface thermal resistance conditions. Among them, the solid line, the dashed line, and the dotted line respectively show the FEM simulation with no interface thermal resistance, low interface thermal resistance, and high interface thermal resistance. The primitive experimental measurement results with small error bars are completely distributed in the middle area between low interface thermal resistance and high interface thermal resistance. After considering the influence of effective interface thermal resistance, it is apparently observed that the ETC is significantly greater than PETC, and a more obvious

abnormal enhancement and normal reduction in ETC has been observed. (e) The relative change factors of enhancement configuration and reduction configuration, which have a very good correspondence with the theoretical prediction. The dotted line gives the relative change of the mean effective thermal conductivity for the different temperature difference case.

**Table S1**

Effective interface thermal conductivity ( $\text{Wm}^{-1}\text{K}^{-1}$ )			
	$\Delta T = 60\text{K}$	$\Delta T = 40\text{K}$	$\Delta T = 20\text{K}$
<b>Largest-ETC configuration</b>	<b>0.25</b>	<b>0.23</b>	<b>0.23</b>
<b>Uniform configuration</b>	<b>0.21</b>	<b>0.23</b>	<b>0.20</b>
<b>Smallest-ETC configuration</b>	<b>0.31</b>	<b>0.47</b>	<b>0.26</b>

**Table S2**

MLP structure optimization results				
Structure of the MLP	Performance	$R_{\text{training}}$	$R_{\text{validation}}$	$R_{\text{all}}$
<b>32 32 32 16 1</b>	<b>0.000171</b>	<b>0.98692</b>	<b>0.98186</b>	<b>0.98603</b>
<b>32 32 16 4 1</b>	<b>0.000442</b>	<b>0.96581</b>	<b>0.9596</b>	<b>0.96471</b>
<b>32 16 8 1</b>	<b>0.00149</b>	<b>0.87876</b>	<b>0.86981</b>	<b>0.87718</b>
<b>32 16 4 1</b>	<b>0.00163</b>	<b>0.86716</b>	<b>0.86024</b>	<b>0.86593</b>
<b>32 8 4 1</b>	<b>0.00318</b>	<b>0.71747</b>	<b>0.71253</b>	<b>0.71659</b>

### Section S3 Highly anisotropic porous structure with extended blocks

In this section, the porous configurations with more periodic units, different number of layers and blocks are constructed, studied and shown in Fig. S12. As the block becomes larger, structural anisotropy ratio can be as high as 40 when the number of units in the block is 10. The associated normalized thermal flux, relative change factor, overall anisotropy ratio, and structural anisotropy ratio under different structure ratio and different material anisotropic ratio are shown in Fig. S13 in detail.

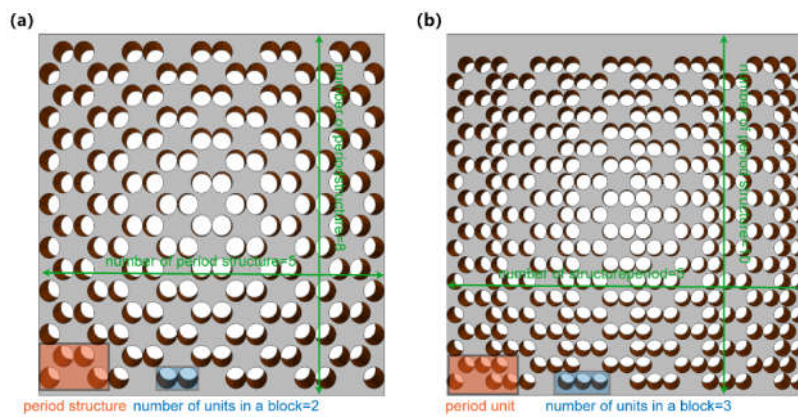


**Figure S12.** Schematic illustration of the highly anisotropic porous structure of the extended block used in FEM calculation. Figure (a) and (b) show the expanded-block porous configurations with 2 and 3 units in a block, respectively, where they have a period number of 5 in the x-direction and full fill in the y-direction.

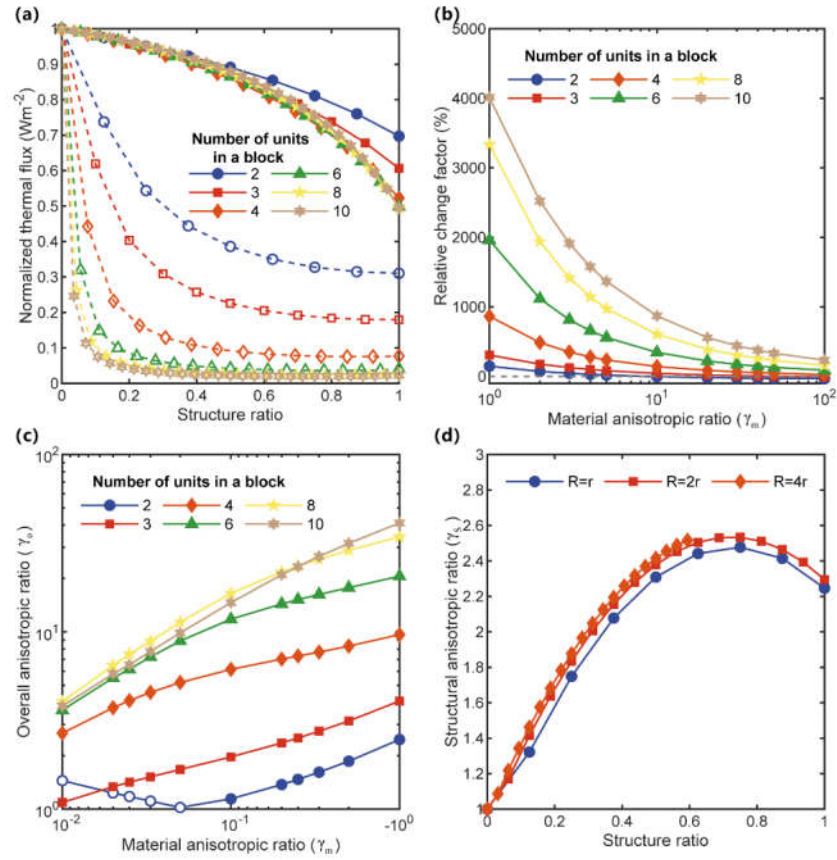


**Figure S13.** Anisotropy properties of porous materials with extended block. (a) The normalized thermal flux as a function of structure ratio for different number of units in a block. The solid dots and lines represent the thermal flux in the x-direction, while the hollow dots and dashed lines represent the thermal flux in the y-direction. (b) The relative change factor as a function of material anisotropic ratio for different number of units in a block. (c) The overall anisotropic ratio as a function of material anisotropic ratio for different number of units in a block. It is worth noting that the value corresponding to the hollow point here is the reciprocal of the overall anisotropic ratio ( $\gamma_o^{-1}$ ). (d) The structural anisotropic ratio as a function of structure ratio under different radius of the porous materials.

#### Section S4 What did the MLP learn?

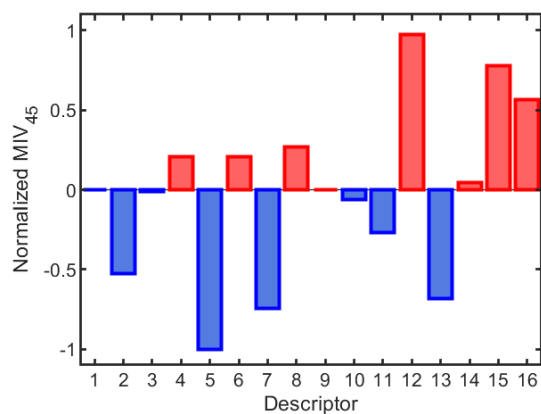
Since the MLP has a high accuracy in describing the functional relationship between the disordered porous configuration and its ETC, what features can it find? We use the mean influence value (MIV) to analyze the contribution of every chain between neurons in MLP and the calculation method of the MIV is as follows:

$$MIV_{ij} = f_{MLP,ij}(\mathbf{A}_i + 10\%\mathbf{A}_i) - f_{MLP,ij}(\mathbf{A}_i - 10\%\mathbf{A}_i). \quad (S10)$$

Here,  $f_{DND,ij}$  represents the function between the input of the  $i$ -th layer and the output of the  $j$ -th layer in MLP, and  $\mathbf{A}_i$  represents the input of the  $i$ -th layer in MLP. One important parameter is  $MIV_{45}$  between the hidden layer 4 and the output layer 5, which directly represents the contribution of the 16 features learned by the MLP, and the normalized  $MIV_{45}$  is shown in Fig. S14. The contribution of different features in the MLP to the ETC is different, so we then calculate  $MIV_{14}$  to study the geometric properties of each feature one by one. A vivid schematic diagram of  $MIV_{14}$  is shown in Fig. S15, here, the length of each arrow indicates the strength of the contribution of moving a unit distance in this direction to ETC, and the red and blue dots indicate the positive and negative contributions, respectively. In order to make features orthogonal to each other, the principal component analysis method is used, and an unexpected combination of characters is also realized at the same time. Subsequently, we move the positions of the pores to the extreme, a graphical representation of each feature learned is shown in Fig. S16. Many local, fragmentary and irregular characters can be easily recognized in each feature. And these fragmentary and irregular knowledge are learned by MLP, and are cleverly combined to achieve a fairly high-accuracy function fitting. This also tells us that MLP can capture many physical mechanisms contained in fragmented features and achieve unexpectedly good results.



334



335 **Figure S14.** The normalized  $MIV_{45}$  between the hidden layer 4 and the output layer 5. We use a histogram  
 336 to show the normalized mean impact value  $MIV_{45}$  between the hidden layer 4 and the output layer 5. Red  
 337 indicates positive correlation and blue indicates negative correlation. It is easy to find that different features  
 338 contribute differently to effective thermal conductivity.

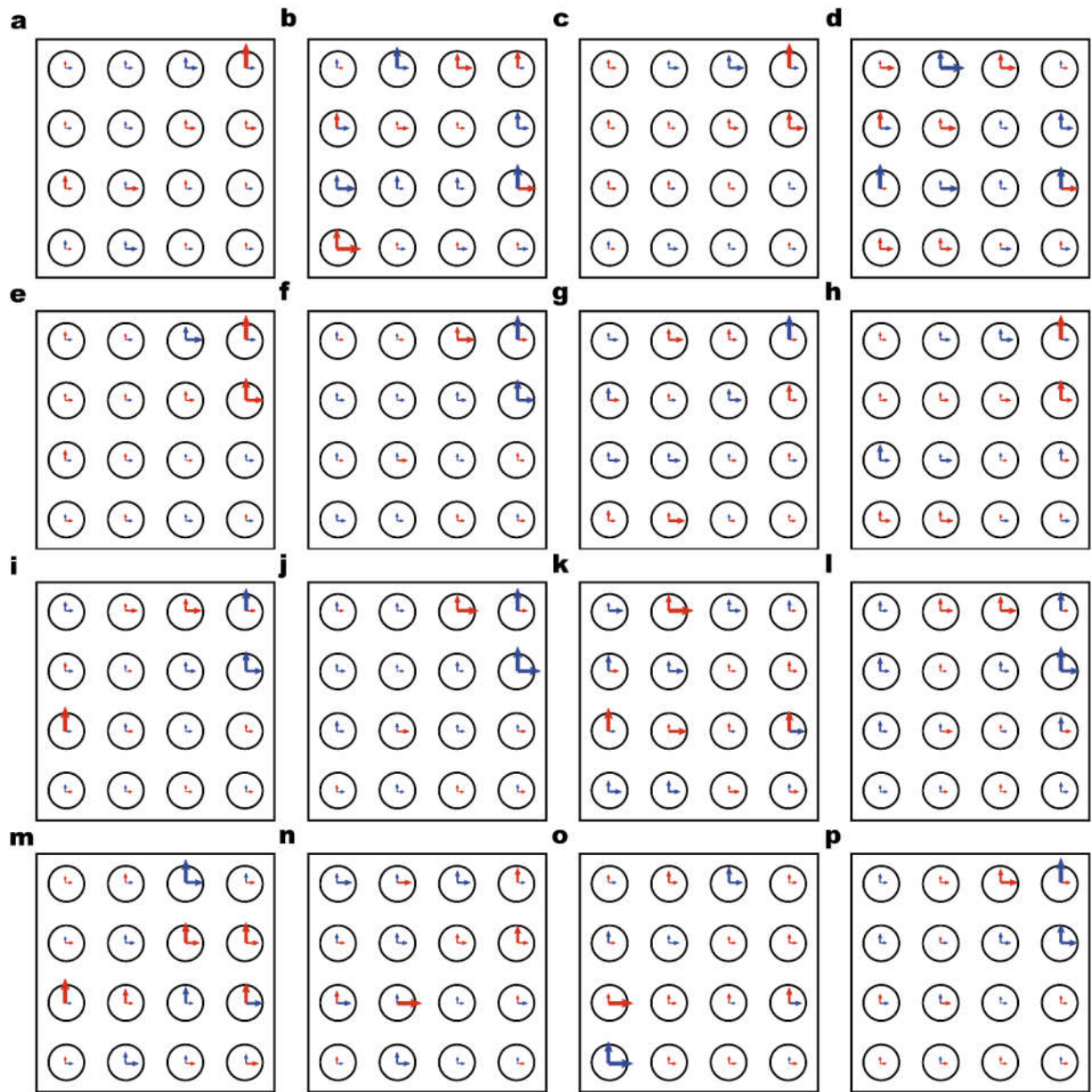


**Figure S15.** The features of the effective thermal conductivity learned by the MLP. Figure (a) to Figure (p) respectively show the characteristics of the 16 features learned by the MLP from the optimal ordered configuration. The length of each arrow indicates the strength of the contribution of moving a unit distance in this direction to ETC, and the red and blue dots indicate the positive and negative contributions, respectively.

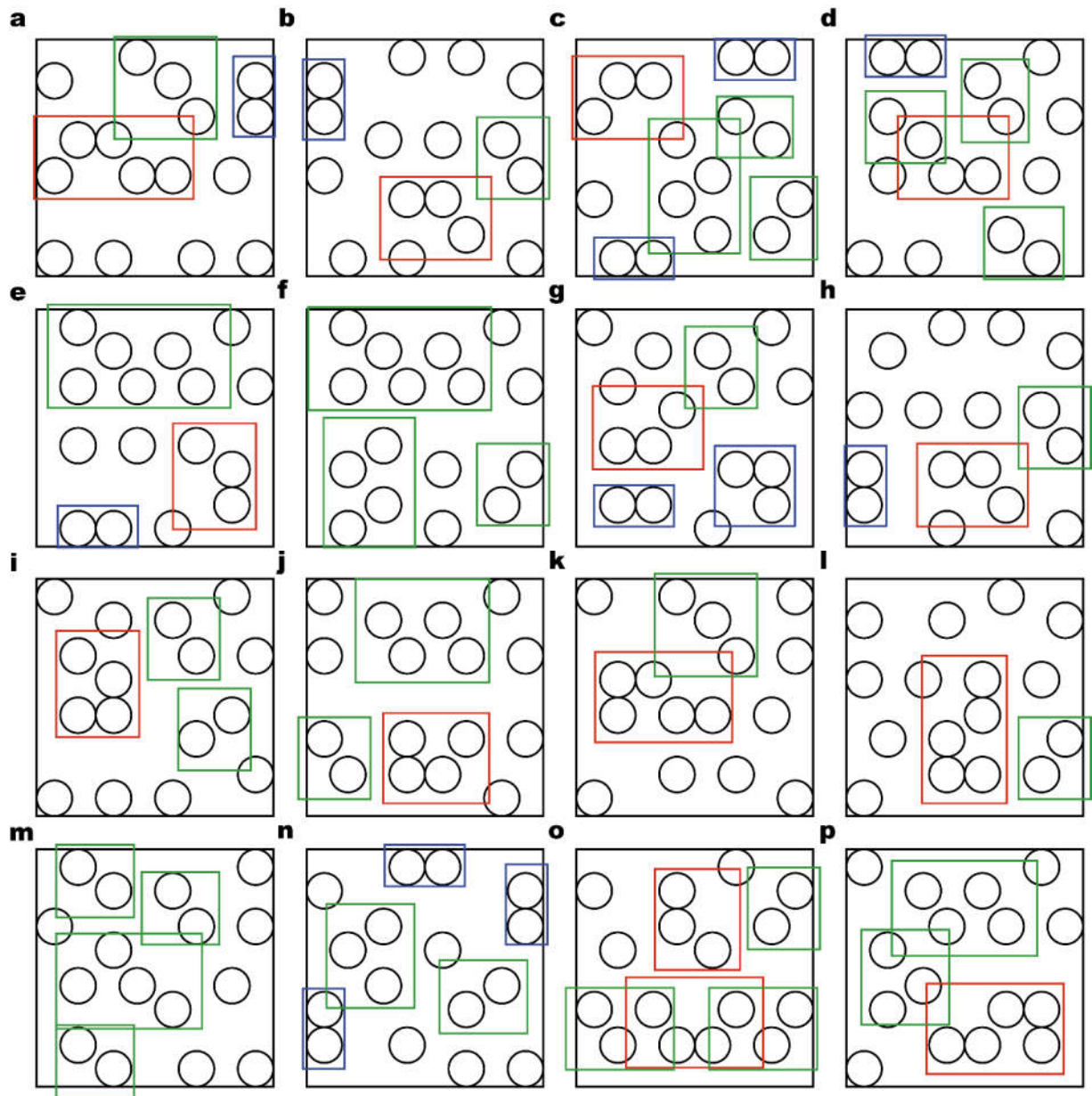


**Figure S16.** The schematic diagram of features of the largest thermal conductivity configuration learned by the MLP after PCA processing. Figure (a) to Figure (p) respectively show the characteristics of the 16 features learned by the MLP from the largest-ETC configuration after PCA processing. Here, we divide these features into high-level character (red), diagonal connection character (green), and parallel connection character (blue).

## REFERENCES

1. Tang GH, Bi C and Fu B. Thermal conduction in nano-porous silicon thin film. *J Appl Phys* 2013; **114**: 184302.
2. Fu B, Tang GH and Bi C. Thermal conductivity in nanostructured materials and analysis of local angle between heat fluxes. *J Appl Phys* 2014; **116**: 124310.
3. Wei H, Bao H, and Ruan XL. Genetic algorithm-driven discovery of unexpected thermal conductivity enhancement by disorder. *Nano Energy* 2020; **71**: 104619.